Available online at www.sciencedirect.com
ScienceDirect
Procedia Engineering 130 (2015) 711 – 730
Procedia Engineering
www.elsevier.com/locate/procedia

14th International Conference on Pressure Vessel Technology

The Effects of Crack Ellipticity on the Mode I SIFs of a Simulated Eroded Pressurized Cylinder

Q. Ma[a,]*, C. Levy[b], M. Perl[c]

[a]*Edward F. Cross School of Engineering, Walla Walla University, College Place, WA 99324, USA*
[b]*Dept. of Mechanical and Materials Engineering, Florida International University, Miami, FL 33199 USA*
[c]*Pearlstone Center for Aeronautical Engineering Studies, Dept. of Mechanical Engineering,*
Ben Gurion University of the Negev, Beer Sheva 84105 ISRAEL

Abstract

The three dimensional stress intensity factors (3D SIFs) of a pressurized cylinder can be greatly affected by many factors. While an autofrettage process may introduce favorable residual stresses on the bore of the cylinder, other factors such as erosions and cracks, once introduced, may greatly reduce the effectiveness of the autofrettage. In this study, a closer look was given to problems with different crack configurations. Effort was expended to evaluate how the ellipticity of cracks affects the overall fatigue life of a simulated eroded pressurized cylinder in comparison with circular crack only configurations. Numerical analysis was performed using ANSYS, a standard commercially available finite element package. The residual stress due to any autofrettage process was simulated using the equivalent thermal loading. In-depth discussion was given to results when cracks of different ellipticity interact with other parameters including the depth of crack and the geometrical configurations of erosion. Specific cases considered include: crack ellipticity a/c=0.5, 1 and 1.5; relative crack depth a/t=0.01-0.2; relative erosion depth d/t=0.05; erosion relative finite length Le/L=0.12-1; erosion ellipticity d/h=0.3-2. Relevant non-erosion results are used for the sake of comparison.

Peer-review under responsibility of the organizing committee of ICPVT-14

Keywords: Stress Intensity Factors; Crack Ellipticity; Thermal Loading; Autofrettage; Bauschinger Effect;

---

* Corresponding author. Tel.: (509)527-2537; fax: (509)527-2867.
E-mail address: qin.ma@wallawalla.edu

Peer-review under responsibility of the organizing committee of ICPVT-14
doi:10.1016/j.proeng.2015.12.172

Nomenclature

a	crack length
d	erosion depth
Le	half length of the erosion groove
L	half length of the cylinder
E	Young's modulus
h	half-width of erosion
K_I	mode I SIF
K_{Ieff}	mode I effective SIF
K_{max}	maximum value of K_{Ieff}
K_{IA}	mode I SIF due to autofrettage
K_{IP}	mode I SIF due to inner pressure
K_{00}	normalizing SIF for effective SIF
P	internal pressure in cylinder
r′	arc erosion radius
R_i	inner radius of cylinder
R_o	outer radius of cylinder
t	cylinder wall thickness

GREEK SYMBOLS

ε	level of autofrettage
ν	Poisson's ratio
σ_y	yield stress

1. Introduction

In a wide range of industries such as power, chemical, food preparation, nuclear, renewable energy, and armament industries, thick-walled pressurized cylindrical vessels have been used as, but not limited to, industrial boilers, nuclear reactors, high-pressure containers, and gun barrels. When typical thick-walled high pressure vessels are subjected to severe environmental conditions, such as gun barrels under repetitive high pressure pulses, acute temperature gradients, and corrosive environment of the combustion gases resulting from the firing process, axial erosions can be practically developed on the inner surface of the barrel and cracks initiated, typically, from or near the deepest lines of the erosion surfaces (DLES).

Autofrettage is the typical process that has been utilized for over a century on thick-walled cylindrical pressure vessels in order to introduce favorable residual compressive stresses at the inner portion of the cylinder's wall (Kendall [1]). The compressive stresses at the bore due to the autofrettage process allow a higher operational pressure in the vessel and decrease cylinder susceptibility to possible inner cracking by impeding crack initiation, further slowing down fatigue crack growth, and thus possibly extending the pressure vessel's fatigue life.

Previous work by Levy et al. and Perl et al. [2-6] has focused on the investigation of SIFs employing an "ideal" autofrettage residual stress field based on Hill's solution [7]. Hill assumed that the cylinder was made of an elastic-perfectly-plastic material, ignoring the Bauschinger Effect (BE), and using the von-Mises yield criterion. However, some typical gun barrel alloys exhibit a considerable BE. The BE is named for the phenomenon discovered by Bauschinger [8] for the continuous change of the yield stress due to cyclic loading. He found that for certain materials that have yielded in tension or compression and were subjected to reversed tension (or compression), the subsequent yield stress was often reduced in comparison to the first yield stress.

Attempts have been made to incorporate the *BE* in the fatigue life analysis of the thick-walled pressurized cylinders. For example, Milligan et al [9] studied experimentally the *BE* in a modified 4330 high-strength steel used for gun barrels in the mid 1960's. More recently, Chen [10], Chaaban et al [11], and Parker and Underwood [12], have attempted to incorporate the *BE* into autofrettage analysis. However, none of the models employed was able to simulate the complete nonlinearity of the unloading phase of autofrettage. In 1997, Jahed and Dubey[13] suggested an improved algorithm based on the actual material stress-strain curve. Within the re-yielding zone their numerical model incorporates the varying *Bauschinger Effect Factor (BEF*) which is experimentally determined. This model was further extended by Parker et al [14], and its application by Parker and associates [14, 15] resulted in a more realistic evaluation of the autofrettage residual stress field.

Numerical methods have been employed to study the impact of the *BE* on three-dimensional SIFs using the Parker [15] data. One study evaluated the SIFs for internal radial cracks in a gun barrel with autofrettage [16] and another study investigated internal longitudinally-coplanar cracks in a gun barrel [17]. More recent studies investigated the combined axial and coplanar cracks [18-19]. The SIF due to autofrettage-K_{IA} for a large number of crack configurations was evaluated with and without the *BE*. It was found that the *BE* reduced the beneficial K_{IA} value by up to 56%, as compared to the case of "ideal" autofrettage. Also, the *BE* was found to increase the K_{Ieff} value in some cases by 42-100% compared to their ideal autofrettage counterparts [18-19]. However, none of these studies to date has considered how the *BE* may influence the cracked eroded cylinders.

In the studies of [20, 21], an attempt was made to integrate the *BE* in an eroded cracked pressurized cylinder with multiple axial erosions and one axial edge crack, i.e., using only 2-D geometry for the erosions and cracks. In a more recent study [22], an axial erosion (a 2-D groove) and a finite 3-D crack emanating from the deepest lines of the erosion surfaces (DLES) have been studied to consider the impact of "ideal" autofrettage (without the *BE*), i.e., the *BE* Independent Autofrettage (*BEIA*), versus the "real" autofrettage (with the *BE* included), i.e., the *BE* Dependent Autofrettage (*BEDA*) at full (100%) autofrettage level. Yet, most recent work [23] addressed the effect of finite erosions with limit results and discussions.

In this study, we closely evaluate how the crack ellipticity affects the SIFs when combined with finite 3-D erosions. Because the effective SIFs may vary in different patterns and magnitudes when consideration is given to the combination of crack geometry, crack depth and various erosion geometrical configurations, we focus our discussion for cases of crack front ellipticity, measured by its ellipticity ratio, a/c, when crack depth varies from a/t=0.01 to a/t=0.25. Investigation is undertaken to evaluate how the maximum effective SIFs vary with the finiteness of erosion length, Le/L, and how the a/c curves change in value and order as the crack front extends into the cylinder's thickness. The primary focus in this study is to cases having 5% relative erosion depth and elliptic erosion cases. Arc erosions and their effects on the SIF have been addressed elsewhere.

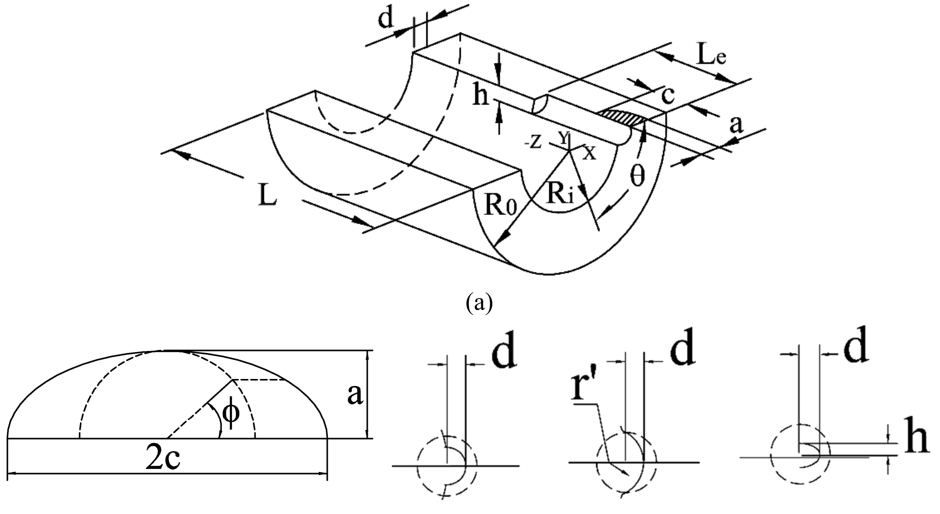

(a)

(b) (c) (d) (e)

Fig. 1. Model of the eroded cylinder with a crack emanating from the erosion DLES; (a) The model of the eroded cracked cylinder with symmetrical planes at Z=0, θ=0 deg and θ=90 deg. (b) The definition of the angle ϕ. Erosion configurations defined: (c) semi-circular; (d) arc; and (e) elliptic erosions.

2. The Mathematical Model

Figure 1 depicts a quarter of the cylinder containing the finite erosion and crack considered in this study. The thick-walled cylinder is assumed to be made of steel with Young's modulus $E=3\times10^4$ksi (206 GPa), Poisson's ratio $\nu=0.3$, and yield stress σ_y=170ksi (1172 MPa). The internal pressure is taken as $p = \sigma_y/3.55$, which is typical of high-pressure applications and which enables comparison with Becker et al. [24], Levy et al. [2], Perl et al. [3,4] and Ma et al. [19]. The internal pressure is applied to the surface of the bore including the eroded surfaces and the crack surfaces. Furthermore, the cylinder is assumed to be fully autofrettaged either through an "ideal" (*BEIA*) process or a more realistic (*BEDA*) process.

For all cases, the cylinder is considered elastic and infinitely long containing a finite axial groove (erosion) of depth *d*, half length of Le and width 2h, at the inner surface of the cylinder and straight fronted. Furthermore, the elastic cylinder has an inner radius R_i, and outer radius R_o, and wall thickness t. Note that the ratio of R_o and R_i is taken as $R_o/R_i=2$ for all our studies.

2.1. Finite Element Idealization

The methodology described here to extract the SIFs was established by Barsoum [25] and Okada et al. [26]. Due to the various symmetries of the geometrical configurations, only part of the cylinder must be analyzed. The planes of symmetry, $Z = 0$, $Z=-L$, $\theta = 0$ *deg*, *and* $\theta=180$ *deg* (see Fig. 1a) allow us to model only part of the cylinder enclosed within them. The cylinder is assumed to freely move in the axial direction as is commonly hypothesized, meaning it is free of loads and unconstrained at its ends. As described elsewhere in this paper, the autofrettage residual stress field for both *Bauschinger Effect Dependent Autofrettage (BEDA)* and *Bauschinger Effect Independent Autofrettage (BEIA)* is simulated by the proper equivalent thermal load.

The model is solved using ANSYS [27], a standard FE code, in two consecutive steps via the submodeling technique. In the first step, a global mesh of the entire segment is generated using 10-node tetrahedron elements while applying a half automatic meshing procedure. The elements are varied in size, small near the crack front and gradually increased when moving away from it as shown in Fig. 2(a) and (b). Figure 2(b) shows the erosion geometry and demonstrates how the mesh density changes as one moves away from the crack front. The displacements obtained from the global mesh are used as boundary conditions for the submodel in the second stage.

In the second step, a toroidal submodel is created covering the crack front area with three layers of 20-node isoparametric elements as shown in Fig. 2(c). Elements collapsed to wedges form the singular elements at the crack front [25, 26] for the first layer as well as two additional element layers above the first layer. The displacements from the global solution act as boundary conditions to the outer surface of the third layer. A comparison between the stress fields on the interface surface of the global and the submodels is performed to ensure a smooth transition between the two stages.

Convergence tests were performed using the stress intensity factor as the convergence criterion. Based on these trials, it is anticipated that the level of error will be less than 5% for meshes of more than 20,000 degrees of freedom (DOF) for most cases. Typical meshes included about 10 thousand elements with 16 thousand nodes. The option where the software automatically adjusted elements shape and aspect ratio for all meshes was always chosen.

SIFs are calculated from the submodel results using the code's crack-face displacement extrapolation procedure. The SIFs were calculated every 9 degrees from ϕ= 0 deg to 90 deg (see Fig. 1b). The results of the present model were validated against K_{Ieff}, K_{IP}, and K_{IA} values obtained by Perl [4, 5] and Levy et al. [6] for "ideal" autofrettage. All the results were found to be in excellent agreement.

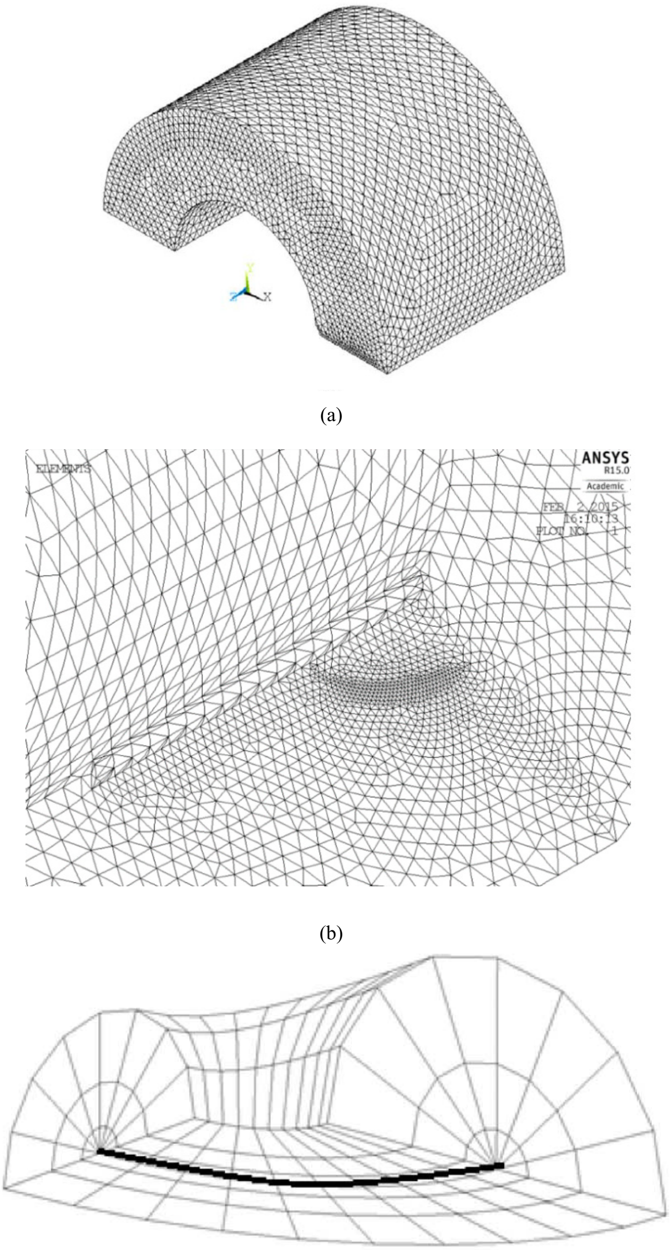

(a)

(b)

(c)

Fig. 2. The Finite Element Model; (a) a typical global mesh; (b) a typical mesh at the vicinity of the crack front; (c)The crack submodel showing the toroid-like finite element mesh with the thick black curve to indicate where the crack front is located.

2.2. Autofrettage and Its Thermal Equivalent Simulation

As previously mentioned, in order to enhance the fracture endurance of pressure vessels, favorable residual stresses are often introduced by the autofrettage process. When radial cracking occurs at the cylinder's inner surface, these stresses cause usually a negative SIF, K_{IA}, which lowers the total K_I at the crack tip, thus reducing its growth rate under cyclic loading. Based on the assumption of von Mises yield criterion, the incompressibility conditions, and an elastic-perfectly plastic material, the plane-strain stress distribution for an ideal autofrettage cylinder is given by Hill [7]. Pu and Hussain [28] implemented a temperature field in a finite element analysis of a cracked autofrettaged cylinder to simulate the autofrettage effect. They have demonstrated that the thermal loading not only actually reproduces the residual stresses due to autofrettage in the intact vessel, but also simulates their redistribution accurately once the cylinder cracks. Therefore, the most feasible way to incorporate these residual stresses, which are continuously redistributed due to the changing geometry, is to simulate them by active thermal loading. The thermal loading simulation process is described in detail in Perl and Aroné [29] and in Perl [30].

Parker's [15] $\mathcal{BEDA}$ field is given numerically in terms of the residual hoop stress values at discrete points throughout the cylinder's wall. Perl [30] provided an exact numerical algorithm that enables the direct evaluation of the equivalent temperature field for simulating any analytically or numerically expressed autofrettage residual stress field. Recently, Levy et al. [17] has successfully applied Perl's algorithm to predict Parker's $\mathcal{BEDA}$ residual stress field. Therefore, the equivalent thermal load obtained by Levy et al. [17] for Parker's discrete residual stress field has been adopted in this study for evaluating the $\mathcal{BEDA}$ SIFs at the autofrettage level ε=100%.

Although the introduction of the erosion(s) cause(s) a high stress concentration at its deepest point, the hoop stress (which at this point is equal to the von Mises effective stress) resulting from the process of autofrettage, in either $\mathcal{BEIA}$ or $\mathcal{BEDA}$, can reach at most σ_y [2-3, 22]. Thus, in the presence of the erosion(s), complete residual stress redistribution occurs. The new residual stress field is found to be similar to that of a fully autofrettaged non-eroded cylinder of inner radius $R_i'=R_i+d$ and outer radius R_o. Therefore, it is better to superimpose the SIF for the eroded internal pressure cases on the non-eroded autofrettage cases to obtain a realistic SIF for an eroded cylinder under combined internal pressure and autofrettage [24]. We now see that the approximation for K_{IA} in an eroded cylinder is solely dependent on the erosion depth and is independent of its shape. This simplification allows us to obtain the K_{IA} values with much less computational time and effort while still yielding conservative results. In this paper, for the sake of conciseness, only normalized combined SIFs will be presented for discussion.

2.3. Normalized Effective SIFs and Their Normalizers

Stress intensity factors, K_{IP}, K_{IA} and $K_{Ieff} = K_{IP} - | K_{IA} |$ are obtained for various combinations of erosion and crack geometrical configurations as mentioned in the previous sessions. In order to enable superposition of the pressure and autofrettage of both $\mathcal{BEIA}$ and $\mathcal{BEDA}$ cases, all K_{IP}, K_{IA} and K_{Ieff} and K_{max} are normalized with respect to

$$K_{00} = p\sqrt{R_i} \tag{1}$$

By using the normalizer (1), all the effective maximum SIFs can be compared without concern for crack configurations to complicate the analysis.

3. Results and Discussion

3.1. SIF Distribution Pattern along the 3D Crack Front Affected by Crack Depth

SIF distribution pattern along the 3-D crack front was well documented previously in literature. However most of the previous discussions focused on the SIF patterns for pressure cases only [31,32] or for cases affected by $\mathcal{BEIA}$ and/or $\mathcal{BEDA}$ conditions with limited information that concern cases usually with only fixed crack depth of relative crack depth a/t=0.05 and semi-circular erosion of relative erosion depth d/t=5% [23]. Since the shape of the SIF pattern affects fundamentally how and where the maximum SIF occurs, we present two cases in this writing to illustrate how the SIF pattern is affected not only by the crack ellipticity but also by the crack depth (and possibly by erosion depth as well, but not included in this discussion) and the materials properties.

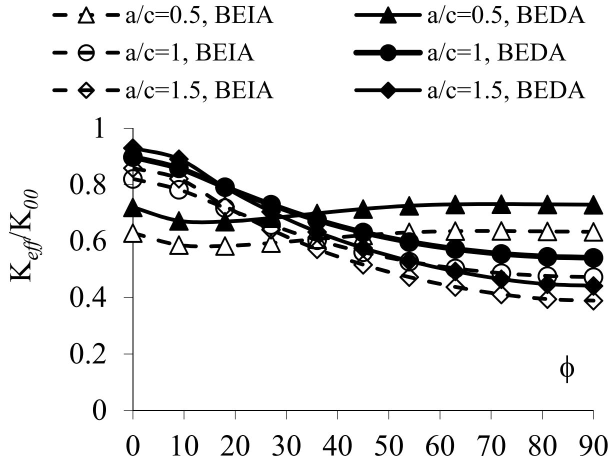

Fig. 3. The SIF distribution along the crack front for a cylinder that contains a straight-through semi-circular erosion (d/h=2 & Le/L=1) of constant depth (d/t=0.05) and a shallow crack a/t=0.01with three different shapes a/c=0.5, 1 and1.5.

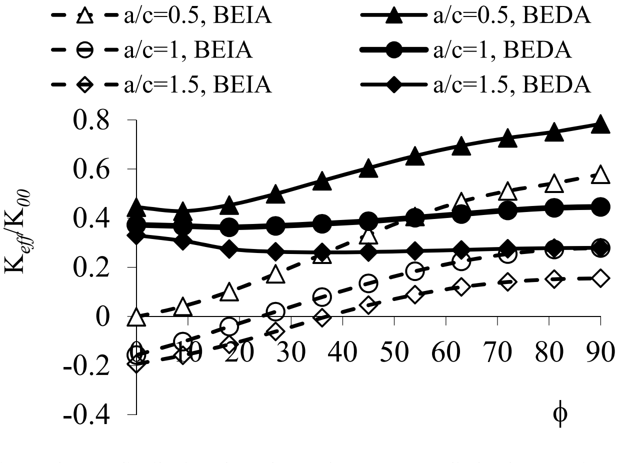

Fig. 4. The SIF distribution along the crack front for a cylinder that contains a straight-through semi-circular erosion (d/h=2&Le/L=1) of constant depth (d/t=0.05) and a deep crack a/t=0.25 with three different shapes a/c=0.5, 1 and1.5.

For a typical very shallow crack case, Fig. 3 provides a plot of the normalized effective SIFs along the 3D crack front. It represents the normalized effective SIF distributions along the front of a semi-circular shallow crack of relative depth a/t=0.01, originating at the DLES of the erosion with relative length Le/L=1 in an autofrettaged pressurized cylinder with (*BEDA*) or without (*BEIA*) Bauschinger effect. All the solid continuous curves with solid symbols represent the results of *BEDA* while all the dashed curves with open symbols represent the results of *BEIA*.

We see that the maximum SIFs occur either at ϕ=0 deg or at ϕ=90 deg depending on what the crack configuration is. For the cases of a/c=1 and 1.5, the maximum SIFs occurs at ϕ=0 deg and the SIF values decrease with the increase of the angle. This is because K_{Ieff} at ϕ= 0 deg is more amplified than K_{Ieff} at ϕ= 90 deg due to the fact that the stress concentration decreases away from the DLES, as discussed by Perl et al. [4]. This trend of the curve is reversed for the case of a/c=0.5. Whatever the crack configuration, the SIFs are all significantly affected by the presence of the Bauschinger effect. This is apparent by noticing the fact that all the corresponding results of *BEDA* are higher than their counterparts of *BEIA* cases. For instance, for all the eroded cases considered herein, the *BEIA* underestimates the values of K_{Ieff} in the range of 8-13% with respect to their counterparts. This indicates that the Bauschinger effect impacts the SIFs significantly and therefore it must be considered in order to evaluate the fatigue life of such pressurized autofrettaged cylinders more accurately [23].

Figure 4 demonstrates how different the SIF distribution pattern is from the previous one. For deep cracks, the crack ellipticity has the most significant effect on its overall SIF trend. Consider the fact that the stress concentration decreases away from the DLES as discussed by Perl et al. [4] for cases of a/c≥1. This fact is true for a pressure alone case as well as for the autofrettage case. Therefore when a combined case of pressure and autofrettage is considered, the SIF pattern becomes more complicated and its trend depends on the competing SIF trends away from the DLES between the pressure and the autofrettage. Figure 4 reflects such a complexity that is not discussed previously. In this figure, all the solid symbols are again the *BEDA* cases. We observe that all the counterpart *BEIA* cases are significantly lower that the *BEDA* cases. The underestimation of the SIF values by the *BEIA* counterpart is between 26-159% along the crack front for various cases. This means that if the K_{Ieff} is larger by 159 percent, then the fatigue life will be shorter by about $(1/1.59)^3$=0.25. In the meantime, we see that the trend of all the *BEIA* cases demonstrates that all the maximum effective SIFs are located at ϕ= 90 deg even for those cases of crack ellipticity a/c≥1. There is similar trend for the *BEDA* cases but not as pronounced as the *BEIA* cases. For example, for the cases of a/c=1.5, the maximum effective SIF for this case is actually located at ϕ= 0 deg and then the SIF decreases away from the DLES. We also see that negative values of the K_{Ieff} are present for *BEIA* cases. This simply indicates that the crack is closed and the crack propagation is not possible under the *BEIA* condition at these crack front locations.

3.2. The Effects of Crack Ellipticity on Shallow Cracks Emanating from Elliptic Erosions

Figures 5-12 overall demonstrate how the crack ellipticity affects the maximum effective SIFs when crack depth is shallow a/t≤0.05 and when the cylinder is with the presence of elliptic erosions. For all the elliptic erosion cases used in this writing, the SIFs are evaluated at the constant erosion depth to wall thickness ratio, d/t=0.05. The erosion ellipticity, d/h, is in the range of 0.3 and 2. A semi-circular erosion is represented by d/h=1. When the value of d/h increases, the erosion becomes narrower but the depth of the erosion is kept constant.

Figure 5 shows how the normalized maximum SIFs vary as a function of the relative erosion length Le/L and the degree of crack ellipticity a/c = 0.5-1.5 for a very shallow crack of relative depth a/t=0.01. The erosion is the shallowest erosion of ellipticity of d/h=0.3 among all the cases studied herein and with a depth of 5% wall thickness.

It can be seen that the maximum effective SIFs always increase with the increase of the relative erosion length Le/L. However, the increase of the maximum effective SIFs become much less dramatic when the erosion length is larger than Le/L=0.2. This makes sense simply because the smaller the erosion ellipticity, the shallower the erosion becomes which reduces the stress concentration, in general, near the crack location and makes the erosion length less significant to the change of the SIF magnitude. This observation is similar to the effect of those arc erosions when the erosion arc radius is large (r′/t=0.3) as discussed elsewhere in a companion paper.

The effect of the degree of crack ellipticity appears not as significant as other factors that affect the magnitude of the effective SIFs. At the same Le/L along the axis of the entire relative erosion length Le/L, the largest values of the maximum effective SIFs rest on the crack ellipticity a/c=0.5 while the lowest values are on the a/c=1.5 curve. The values of the maximum effective SIFs on the a/c=1.5 curve are still about 10-15% lower in comparison with those on the a/c=0.5 curve except that at the non-eroded case. Therefore the effect of the crack ellipticity is still significant enough to be distinguished even for this very shallow crack and very shallow erosion case. This holds true roughly for both *BEIA* and *BEDA* cases. However the *BEIA* values are always much lower than their *BEDA* counterparts in the range of 24-35%, except for the non-eroded Le/L=0 case, which is even lower at about 82%.

Similar to Fig. 5, Fig. 6 shows results of the normalized maximum effective SIFs for a cylinder that contains a very shallow crack a/t=0.01, a constant erosion depth d/t=0.05 with a *large* erosion ellipticity ratio d/h = 1, which is corresponding to the semi-circular erosion case.

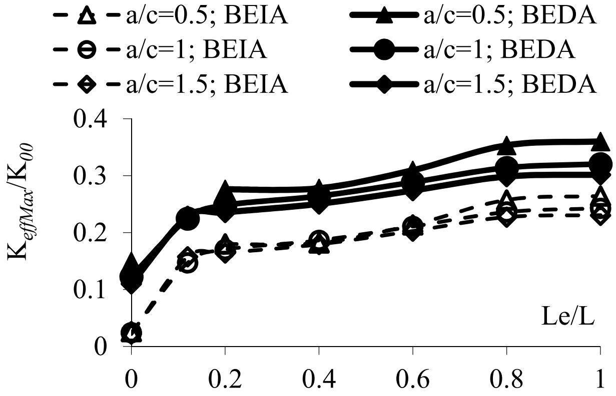

Fig. 5. The effect of crack ellipticity and erosion length finiteness of constant depth (d/t=0.05) on the normalized maximum effective SIFs for a shallow crack of relative crack depth a/t=0.01 and an elliptic erosion d/h=0.3.

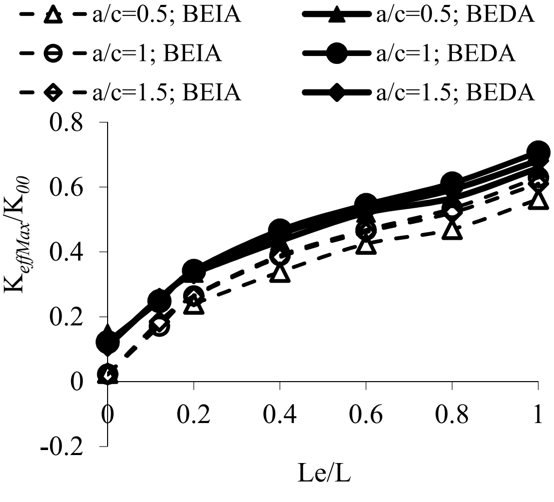

Fig. 6. The effect of crack ellipticity and erosion length finiteness of constant depth (d/t=0.05) on the normalized maximum effective SIFs for a shallow crack of relative crack depth a/t=0.01 and an elliptic erosion d/h=1.

It can be seen that for all the cases presented herein, the maximum effective SIFs always increase with the increase of the relative erosion length Le/L. And the rising trend of the curves last through the entire relative erosion length range investigated. This is very different from the case when the erosion ellipticity becomes very small such as shown on the previous figure at d/h=0.3, for which the increase of the normalized max effective SIFs becomes much less significant when Le/L>0.2.

How elliptic a crack appears to be is insignificant for some cases in comparison with other factors that affect the magnitude of the effective SIFs. For example, when a/c=1 and 1.5, the effective SIFs are very close to each other for cases having the same autofrettage condition, whether *BEIA* or *BEDA*. However the maximum effective SIFs are in general significantly lower for the a/c=0.5 case compared to the a/c=1 and 1.5 cases. In the meantime, the ideal autofrettage *BEIA* underestimates the max effective SIFs from 10% to 80%. The underestimation decreases significantly with the increase of relative erosion length Le/L.

Figure 7 shows how the normalized maximum SIFs vary as a function of the relative erosion length Le/L and the degree of crack ellipticity a/c = 0.5-1.5 for a very shallow crack of relative depth a/t=0.01 and with the largest erosion ellipticity d/h=2, which represents the most slender erosion among all those studied herein.

The rising trend for this case is very similar to what is observed in the previous figure. However, one may notice a significant difference between Fig. 6 and 7 is the switch in the order of the curves between the a/c=1 and a/c=1.5. In other words, the most dangerous crack configuration for this case is a/c=1.5. The lowest values of the maximum effective SIFs for this case rest on the curve of a/c=0.5 under both *BEIA* and *BEDA* conditions. Taking an example, considering the *BEDA* at a/c=0.5 and at a/c=1, the values on the a/c=0.5 are lower 19-22% than those on the a/c=1. However, the values on the a/c=1 are only lower 3-10% than those on the a/c=1.5 curve. Therefore the a/c=0.5 crack configuration becomes the least dangerous in this case (opposite to what is observed on Fig. 5). Thus, it is of great importance to view the crack ellipticity effect on the maximum effective SIFs when considered in combination with other factors especially those of finite length erosion and erosion ellipticity.

One may see that the increases of the effective SIFs from that of the non-erosion cases are not linear since a much sharper rise is clearly seen from Le/L=0 to Le/L = 0.2. Then the increasing trend of those curves become very mild as shown in Fig. 5 when Le/L>0.2. Taking *BEDA* cases for instance, the normalized maximum effective SIFs increases with an average slope to be between 0.62 and 0.77 from Le/L=0 to Le/L=0.2. However the average slope is only between 0.08 and 0.10 from Le/L=0.2 to Le/L=1 for all the crack configurations investigated in Fig. 5. For those cases presented on Fig. 7, the average slope is between 0.86 and 1.67 from Le/L=0 to Le/L=0.2 while the slope is between 0.51 and 0.63 from Le/L=0.2 to Le/L=1. This demonstrates the rising trend becomes more significant throughout the entire Le/L range when the erosion ellipticity d/h becomes large.

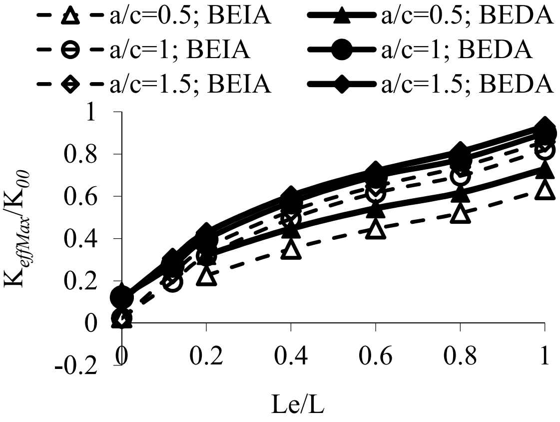

Fig. 7. The effect of crack ellipticity and erosion length finiteness of constant depth (d/t=0.05) on the normalized maximum effective SIFs for a shallow crack of relative crack depth a/t=0.01 and an elliptic erosion d/h=2.

In addition to the rising trend of the normalized maximum effective SIFs, one may notice that there is a missing point at Le/L=0.12 for the case at a/c=0.5 for both *BEDA* and *BEIA* cases. The reason is because the erosion runs into the crack front for this case and the values of the SIFs could not be obtained from the program. At Le/L =0.2 for a/c=0.5, the program again has problems handling the meshing set-up. To preclude this problem the program was run at Le/L=0.21 and that value is given on the graph.

Figure 8 demonstrates how the normalized maximum effective SIFs are affected by the crack ellipticity as a function of the erosion configuration d/h of constant depth d/t=0.05 for shallow cracks of relative crack depth a/t=0.01. The solid curves with solid symbols represent those results when Le/L=0.6. The dashed curves with solid symbols represent those results when Le/L=1, which are the highest curves on the graph. The dashed curves with open symbols represent those results when Le/L=0.2, which are the lowest curves on the graph. It is clear that the maximum effective SIFs increase with the increase of erosion ellipticity ratio, d/h. This is because the larger the ellipticity ratio the narrower the erosion, which causes more severe stress concentration at the tip of erosion and more severe stress field for the nearby crack front, thus increasing the SIF.

In the meantime, it is of no surprise that the a/c curves may cross each other at certain location along the d/h axis. This indicates that any a/c curve may change its dominance when other factors are taken into account. For example, the curve of a/c=0.5 may fall from the highest position to the lowest position along the d/h axis as shown in Fig. 8. This observation is found true for many cases studied herein. This fact is simply the result of the combined effect from the pressure load, *BEDA* and *BEIA* conditions and other multiple factors due to the variation of crack and erosion geometries. Similar observations have been found by Ma et al. [33].

Figures 9 thru 12 show similar results as figures from 5 to 8, but deeper cracks. However These results demonstrate that the effect of the crack ellipticity on the normalized max effective SIFs are more pronounced as the crack deepens, a/t=0.01 for previous cases vs. a/t=0.05 for current ones. This argument is clearly seen when one realizes how more of a spread between the curves exists among different levels of crack ellipticity from a/c=0.5 to 1.5 as shown in Fig. 9 through 12 for both *BEDA* and *BEIA* cases.

Let's take the *BEDA* cases in Fig. 9 as an example. Starting with the non-eroded cylinder, the normalized maximum effective SIFs at Le/L=0 for a/c=1 and a/c=1.5 are 0.28 (solid circle symbol) and 0.29 (solid diamond symbol), respectively, which are approximately the same in magnitude. But the normalized maximum effective SIFs for a/c=0.5 (solid triangle symbol) is much lower in magnitude at 0.18. This trend is kept as the erosion length increases. The normalized max SIFs increases the most up to Le/L=0.2 then the slopes decrease as the erosion length increases. In the region Le/L>0.2, the curve of a/c=1 is 0.7-3.0% lower than the a/c=1.5 curve, but the a/c=0.5 curve is 17.5-23.4% lower than the a/c=1.5 curve. Thus the a/c=0.5 is a much less critical configuration than other crack levels of ellipticity.

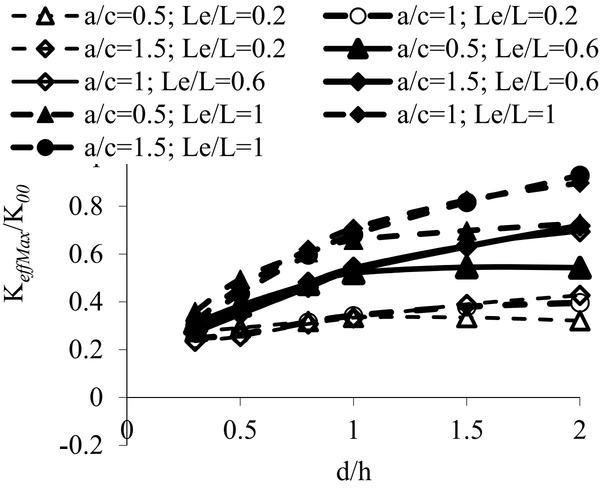

Fig. 8. The effect of crack ellipticity on the normalized maximum effective SIFs as a function of erosion ellipticity of constant depth d/t=0.05, and a shallow crack of relative crack depth a/t=0.01.

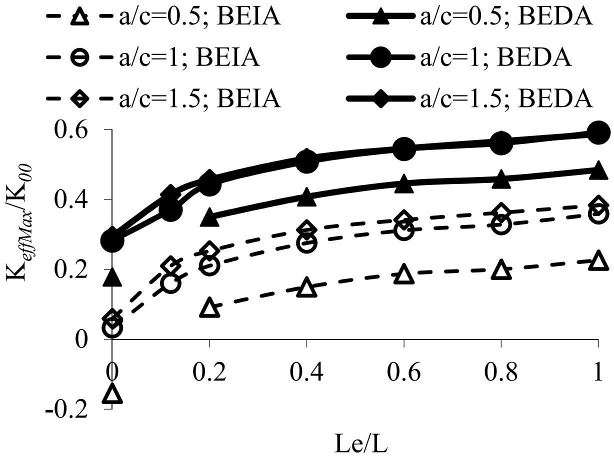

Fig. 9. The effect of crack ellipticity and erosion length finiteness of constant depth (d/t=0.05) on the normalized maximum effective SIFs for a shallow crack of relative crack depth a/t=0.05 and an elliptic erosion d/h=0.3.

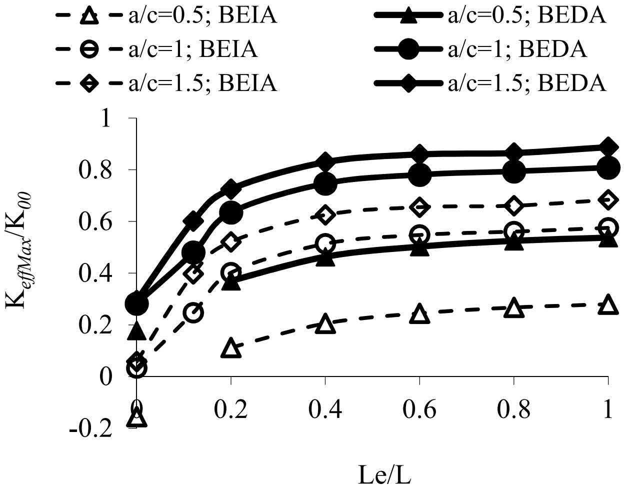

Fig. 10. The effect of crack ellipticity and erosion length finiteness of constant depth (d/t=0.05) on the normalized maximum effective SIFs for a shallow crack of relative crack depth a/t=0.05 and an elliptic erosion d/h=1.

Figures 10 and 11 demonstrate similar behavior of the a/c effect on the normalized maximum effective SIFs as a function of the relative erosion length Le/L when the erosion configuration becomes narrower, i.e., the d/h ratio becomes larger. In comparison with the shallower erosion case shown in Fig. 9, the curves in Figs. 10 and 11 clearly show a much more significant jump from the low SIF values of the non-erosion case to the erosion case when Le/L>0.2. At the same time, we also see that the a/c=1.5 becomes more dominant than and separated from the a/c=1 curve while the a/c=0.5 keeps its much less significant status than the other two crack configurations.

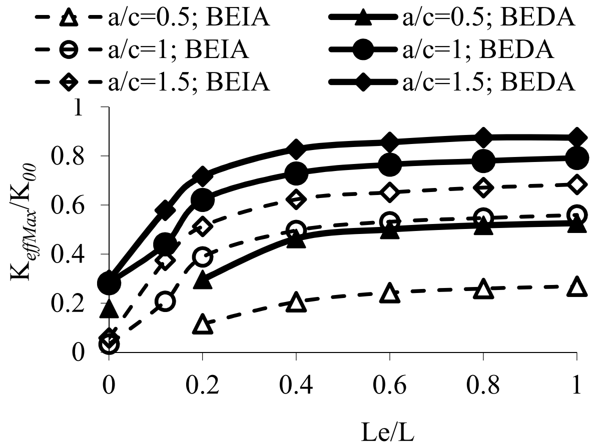

Fig. 11. The effect of crack ellipticity and erosion length finiteness of constant depth (d/t=0.05) on the normalized maximum effective SIFs for a shallow crack of relative crack depth a/t=0.05 and an elliptic erosion d/h=2.

Taking a closer look at Fig. 10, the average slope is between 0.96 and 2.31 from Le/L=0 to Le/L=0.2 while the slope is between 0.21 and 0.22 from Le/L=0.2 to Le/L=1. This again demonstrates the rising trend is only significant when Le/L<0.2. The effective maximum SIFs become much less sensitive when Le/L>0.2. At the same time, taking the *BEDA* and Le/L>0.2 cases, the values of the a/c=1 curve are lower by 8.9% to 12.4% for Le/L=1 and Le/L=0.2, respectively. In the meantime, the values of the a/c=0.5 curve are lower by 39.4% to 48.9% corresponding to Le/L=1 and Le/L=0.2, respectively. This shows that the a/c=0.5 crack configuration produces the lowest crack tip stress severity and is the least harmful to the cylinder life.

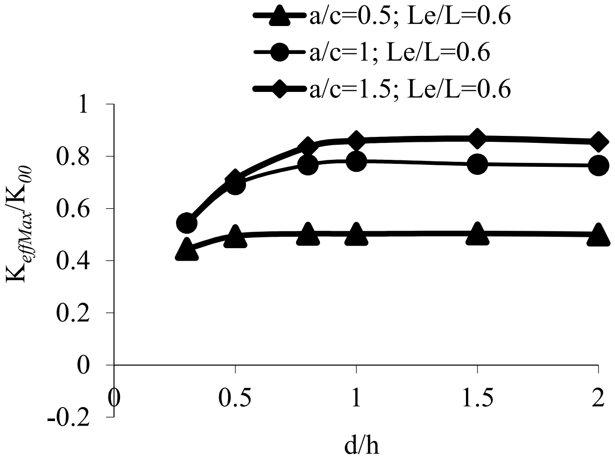

Fig. 12. The effect of crack ellipticity on the normalized maximum effective *BEDA* SIFs as a function of erosion ellipticity of constant depth d/t=0.05, and a shallow crack of relative crack depth a/t=0.05.

The closeness in SIF values of the corresponding graphs between Figs. 10 and 11 demonstrates that the maximum effective SIFs are almost insensitive to the increase of the erosion ellipticity ratio from d/h=1 to d/h=2. This fact is further illustrated on Fig. 12.

Figure 12 shows how the BEDA maximum effective SIFs vary with the erosion ellipticity ratio d/h at Le/L=0.6. As expected, increasing trend is demonstrated on the graph as the increase of d/h ratio. For all the cases, the a/c=0.5 is the lowest while the curves of a/c=1 and 1.5 almost collapse onto each other at the low values of d/h ratio and depart gradually as the d/h ratio increases. We can see that the most dangerous crack configuration is a/c=1.5. In fact, the maximum effective SIFs on the a/c=1.5 curve are 22-71% higher than those on the a/c=0.5 curve.

These results indicate that a small change in erosion length for erosions Le/L<0.2 affect the maximum effective SIFs more significantly for deeper cracks. Crack ellipticity plays an important role on the magnitudes of the SIFs in combination of the erosion finiteness and erosion geometrical configurations. This becomes even more evident when one reads through the subsequent section.

3.3. The Effects of Crack Ellipticity on Deep Cracks Emanating from Elliptic Erosions

Figures 13 thru 16 overall demonstrate how the crack ellipticity affects the maximum effective SIFs when the crack is deep, i.e., at a/t=0.25 and when the cylinder contains elliptic erosions.

Figures 13, 14 and 15 are very much alike. The difference among these three graphs is, in fact, minimal, which indicates the ellipticity effects of the erosions on the maximum effective SIFs are insignificant for very deep crack cases. This observation is further demonstrated in Fig. 16. In this figure, only BEDA results at Le/L=0.6 are shown. Regardless what crack configuration is present, the erosion ellipticity plays almost no role on the magnitude of the max effective SIFs. However different levels of crack ellipticity yields different magnitudes of the SIFs. For instance, the max effective SIFs are the largest for the crack ellipticity a/c=0.5. The other two configurations produce significantly lower maximum effective SIFs. From Fig. 13, in the range of Le/L>0.2, the maximum effective BEDA SIFs are about 39-41% lower for the a/c=1 curve than for the a/c=0.5 curve. However the maximum effective BEDA SIFs are about 45-53% lower for the curve of a/c=1.5 than for the curve of a/c=0.5. Meanwhile, the difference between the a/c=1 and a/c=1.5 curves falls between 11% and 19% depending on the value of Le/L.

The rising trends in Le/L again follow the same observations as discussed previously. Namely, the most significant increase is when Le/L<0.2. As a comparison, for all the cases shown in Fig. 13, the average slope is between 0.60 and 1.17 for Le/L<0.2 while the average slope falls only between 0.04 and 0.09 for cases of Le/L>0.2. This observation holds roughly true for the results shown on Fig. 14 and 15 as well.

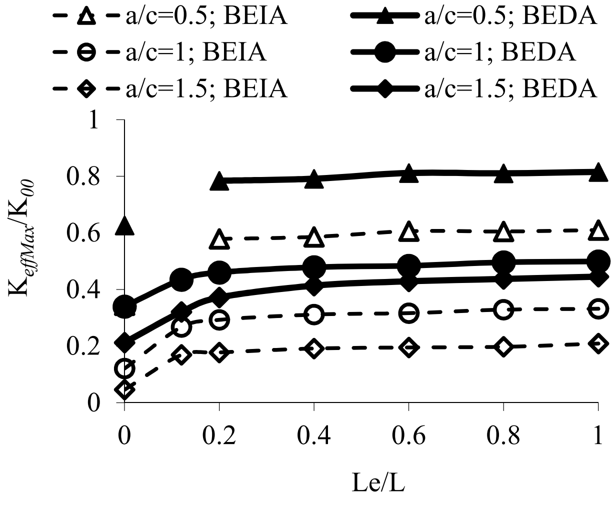

Fig. 13. The effect of crack ellipticity and erosion length finiteness of constant depth (d/t=0.05) on the normalized maximum effective SIFs for a deep crack of relative crack depth a/t=0.25 and an elliptic erosion d/h=0.3.

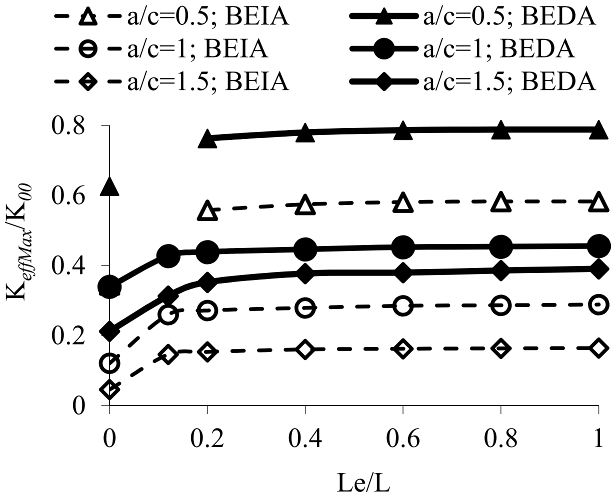

Fig. 14 The effect of crack non-circularity and erosion length finiteness of constant depth (d/t=0.05) on the normalized maximum effective SIFs for a deep crack of relative crack depth a/t=0.25 and an elliptic erosion d/h=1.

It is again worthy to mention that the order of the a/c curves is essentially reversed for the deep crack cases as shown on Figs. 13-16 than those on Figs. 9-12. So the most striking difference observed from Figs. 13-16 in comparison with the previous ones of Figs. 9-12 is the way the crack front ellipticity affects the max effective SIFs. In Figs. 13-16, we see that the a/c=0.5 cases are more critical than the other two configurations of a/c=1 and 1.5 cases, which is an opposite trend to the effect of a/c on the maximum effective SIFs for Fig. 9-12, for example. Thus it appears that at some a/t the a/c curve changes its order. This shall not be a surprise since the combination of crack configurations, crack depth and erosions in addition to pressure and autofrettage are in fact complicated.

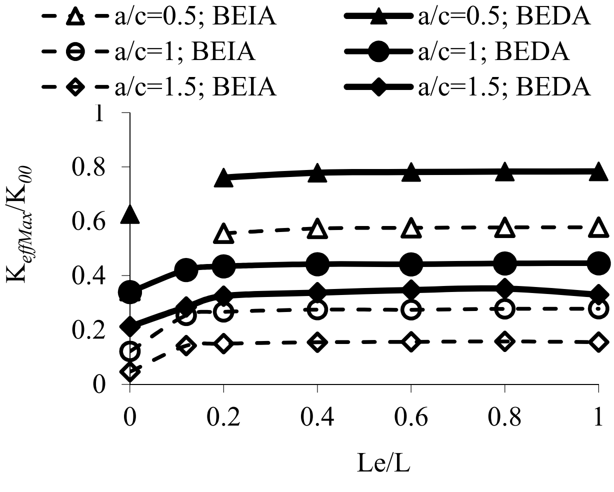

Fig. 15 The effect of crack non-circularity and erosion length finiteness of constant depth (d/t=0.05) on the normalized maximum effective SIFs for a deep crack of relative crack depth a/t=0.25 and an elliptic erosion d/h=2.

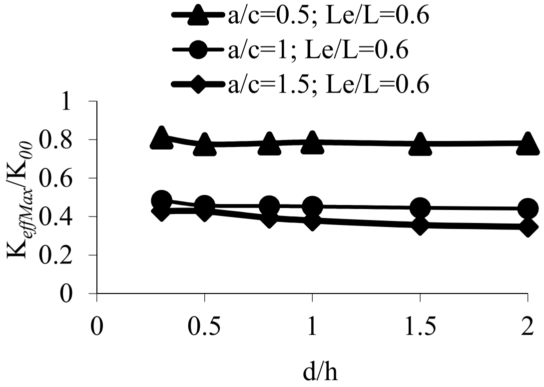

Fig. 16. The effect of crack ellipticity on the normalized maximum effective *BEDA* SIFs as a function of erosion ellipticity of constant depth d/t=0.05, and a deep crack of relative crack *depth* a/t=0.25.

3.4. The Role of Crack Depth on the SIFs

Although the effect of relative crack depth a/t has been discussed throughout this document in combination with other important quantities, it is still significant to set it apart and discuss it in more depth. Figures 17-19 show typical results of the crack depth effect on the maximum effective SIFs for the case of Le/L=1 and d/h=1. The only difference among these three graphs is the crack ellipticity ratio a/c. Regardless of what the a/c values are, the overall impression can be clearly stated such that 1) the maximum normalized SIFs under each pure loading condition always increase with the increase of relative crack depth of a/t. This holds true for the cases either under the pure pressure loading, or under the pure *BEDA* loading condition or under the pure *BEIA* loading condition (here K is taken in absolute value); 2) However, the combined maximum effective SIFs either under *BEDA* or under *BEIA* always increase with the increase of the a/t ratio within a short distance along the a/t axis and then the curve of each combined case decreases with further increase of the relative crack depth a/t. In one case the maximum effective SIFs then increase again as a/t continues to increase (see Fig. 17). Ostensibly, the others will increase as a/t becomes larger than 0.25.

One should be aware that the notation used in this section is slightly different on the graphs from the previous ones. In the previous sections, all the *BEIA* and *BEDA* notations on the graph refer to the combined cases of pressure and autofrettage (either *BEIA* or *BEDA*). In this section those combined cases are listed as the "combined *BEDA*" or the "combined *BEIA*" cases. It is thus used in this section to clarify that each plot demonstrates how the combined *BEDA* and *BEIA* curves are generated from the combination of pressure only SIFs and the autofrettage only SIFs under either *BEDA* or *BEIA* loading conditions. Our goal is to observe the trend of the SIF curves with the increase of the relative crack depth a/t.

Figure 17 plots the normalized maximum SIFs of cases under different loading conditions as a function of relative crack depth of a/t=0.01-0.25. The crack ellipticity is a/c=0.5 which represents the cases of a slender semi-elliptic crack configuration. The thick continuous solid curve with solid square symbols represents the pressure loading only case. As we may see that the normalized maximum SIFs increases continuously with increase of the relative crack depth a/t. The dashed curve with open diamond symbols represents the *BEIA* loading only case and the dashed curve with open circles represents the *BEDA* loading only case. Both dashed curves are indeed "negative" values but they are shown here as their magnitudes.

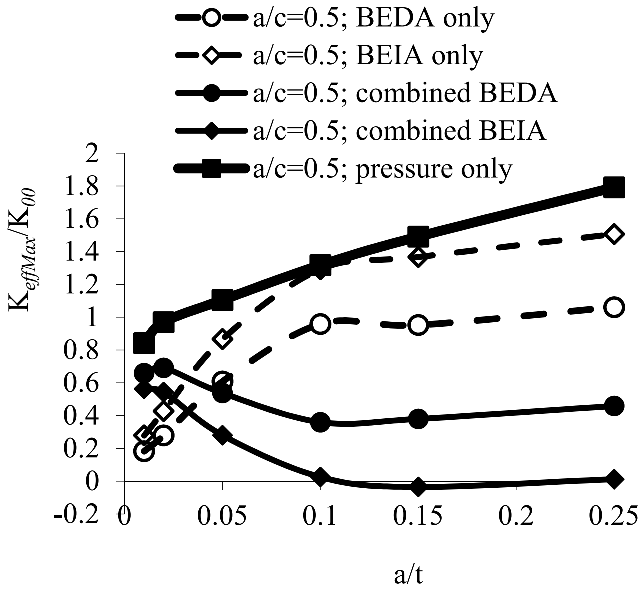

Fig. 17. The normalized maximum effective SIFs as a function of relative crack depth for a *slender semi-elliptic crack a/c=0.5* with a semi-circular erosion d/h=1 of relative erosion depth d/t =0.05 and relative erosion length Le/L=1.

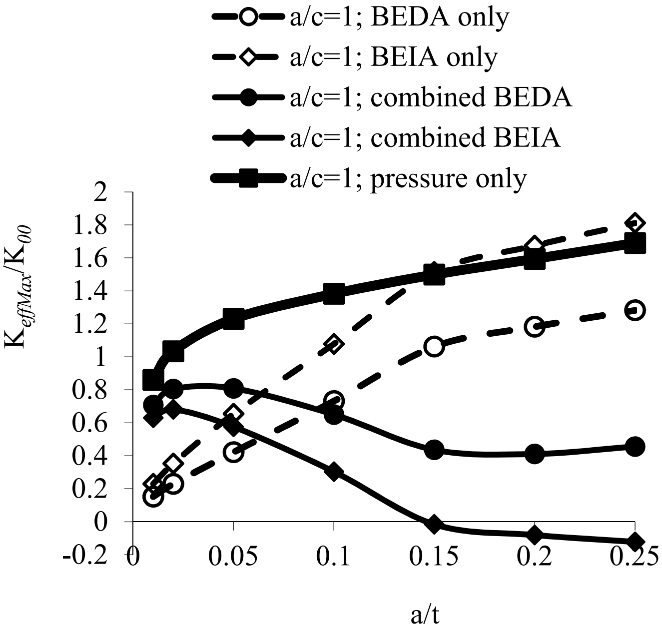

Fig. 18. The normalized maximum effective SIFs as a function of relative crack depth for a *semi-circular crack a/c=1* with a semi-circular erosion d/h=1 of relative erosion depth d/t =0.05 and relative erosion length Le/L=1.

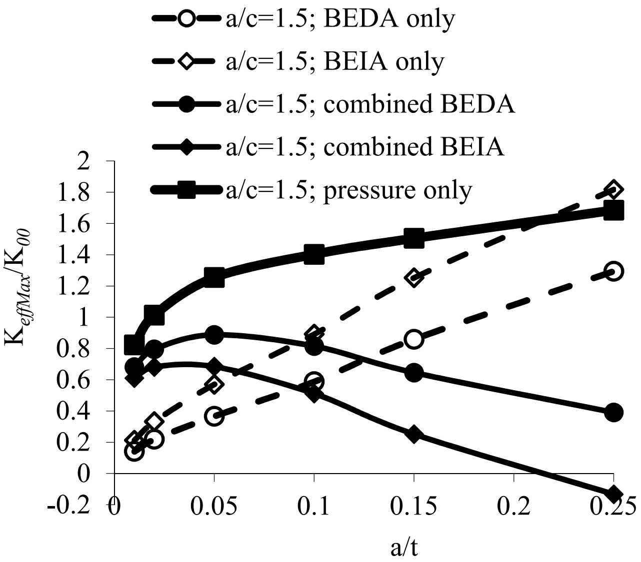

Fig. 19 The normalized maximum effective SIFs as a function of relative crack depth for a *transverse* semi-elliptic crack a/c=1.5 with a semi-circular erosion d/h=1 of relative erosion depth d/t =0.05 and relative erosion length Le/L=1.

As one may see that the *BEIA* loading conditions predict more favorable SIF values since they all generate larger values of the maximum SIFs, which results in prediction of a longer fatigue life. It is also clear that both dashed curves increase with the increase of the relative crack depth a/t in a similar manner as observed for the pressure only case.

The continuous curve with solid circles represents the maximum combined effective SIFs under the combination of the pure pressure loading and the pure *BEDA* loading conditions. The continuous curve with solid diamond symbols represents the maximum combined effective SIFs under the combination of the pure pressure loading and the pure *BEIA* loading conditions. What is interesting is that the combined *BEDA* and the combined *BEIA* cases follow a very different trend on the graph compared to the pure loading (autofrettage or pressure) condition cases. The combined *BEDA* curve increases with the increase of the relative a/t for a relative short crack length when a/t<0.02, then the curve decreases dramatically between a/t = 0.02 and 0.1. After that the curve starts to rise again but very slowly. Similar trend is observed for the combined *BEIA* case. One fact is noted for the *BEIA* case: the maximum combined effective SIFs become negative when a/t>0.1 which predicts closure of crack faces, which is the most conservative prediction of crack propagation.

The symbols used on Figures 18 and 19 are the same as those used on Figure 17. However Fig. 18 shows the results for cases of crack ellipticity a/c=1, which represents cases of a semi-circular crack configuration. Also, Fig. 19 shows results for the cases of crack ellipticity a/c=1.5, which represents cases of a transverse elliptic crack configuration.

While the trends of the pure loading cases on Fig. 18 and Fig. 19 are fundamentally the same as shown on Fig. 17, the combined loading cases show some significant difference from one another. With the increase of the a/t ratio, for all the pure loading cases, the SIF maxima always increase.

On Fig. 18, the combined *BEDA* curve as well as the combined *BEIA* curve show similar trends as in Fig. 17 for similar cases except the kink in the curves occur at a/t=0.15 instead of a/t=0.1 as shown on Fig. 17.

Figure 19 shows that the downturn of the combined *BEDA* and *BEIA* cases are not as dramatic as with the other two figures. Both curves continue to decrease after each reaches its maxima at a/t=0.05 for the combined *BEDA* case and at a/t=0.02 for the combined *BEIA* case.

4. Conclusions

The focus of this study is on the effects of crack ellipticity on the maximum effective SIFs in combination with other geometrical factors and properties. Overall, the erosion reduces the fatigue life of the vessel and the Bauschinger effect compounds this effect, requiring accurate assessment of the maximum effective SIFs. Specifically, the main findings from this research may be summarized as follows:

(a) For shallow cracks of a/t≤0.05, the most critical crack configuration is when the crack ellipticity is a/c=1.5 for the cases investigated herein.
(b) For very deep cracks of a/t=0.25, however, the most critical crack configuration is a/c=0.5.
(c) The most dramatic effect of erosion configuration is when it is very short such that Le/L<0.2 for all cases studied.
(d) Shallow cracks are affected by the erosion more dramatically throughout the entire Le/L regime while deep cracks are less affected and become insensitive for further increase of erosion relative length when Le/L>0.2.
(e) Crack depth plays an important role on the magnitude of SIFs. The maximum effective SIFs increases with the increase of the relative crack depth a/t when a/t =0.02-0.05 depending on which crack elliptic configuration is investigated. But beyond that critical region, with further increase of crack depth, the maximum effective SIFs in general decrease.

Acknowledgements

This work used the Extreme Science and Engineering Discovery Environment (XSEDE), which is supported by National Science Foundation grant number PSC Grant MSS140004P. The first author (QM) acknowledges the support from his University through the Faculty Development Grant.

References

[1] D.P. Kendall, A Short History of High Pressure Technology from Bridgeman to Division 3, Trans. ASME, J. Pressure Vessel Tech., 122 (2000) 229-233.
[2] C. Levy, M. Perl, H. Fang, Cracks Emanating from an Erosion in a Pressurized Autofrettaged Thick-Walled Cylinder—Part I: Semi-circular and Arc Erosions, Trans. ASME J. Pressure Vessel Tech., 120 (1998) 349–353.
[3] C. Levy, M. Perl, H. Fang, Cracks Emanating from an Erosion in a Pressurized Autofrettaged Thick-Walled Cylinder—Part II: Erosion Depth and Ellipticity Effects, Trans. ASME J. Pressure Vessel Tech., 120 (1998) 354–358.
[4] M. Perl, C. Levy, J. Bu, J., Three-Dimensional Analysis of a Semi-Elliptical Crack Emanating from an Erosion at the Bore of anAutofrettaged Pressurized Cylinder, Trans. ASME J. Pressure Vessel Tech., 121 (1999) 1-7.
[5] M. Perl, C. Levy, Q. Ma, The Influence of Multiple Axial Erosions on the Fatigue Life of Autofrettaged Pressurized Cylinders, Trans. ASME J. Pressure Vessel Tech., 123 (2001) 293-297.
[6] C. Levy, M. Perl, Q. Ma, Erosions and Their Effects on the Fatigue Life of Thick-Walled, Autofrettaged, Pressurized Cylinders, Trans. ASME J. Pressure Vessel Tech., 125 (2003) 242-247.
[7] R. Hill, R., The Mathematical Theory of Plasticity, Clarendon Press, Oxford, (1950).
[8] J. Bauschinger, Uber die veranderung der elasticitätsgrenze und des elasticitätsmoduls verschiedener metalle, Zivilingenieur, 27 (1881) 289-348.
[9] R.V. Milligan, W.H. Koo, T.E. Davidson, The Bauschinger Effect in a High Strength Steel, Trans. ASME, J. Basic Eng., 88 (1966) 480-488.
[10] P.C.T. Chen, Bauschinger and Hardening Effects on Residual Stresses in Autofrettaged Thick-Walled Cylinders, Trans. ASME, J. Pressure Vessel Tech., 108 (1986) 108-112.
[11] A. Chaaban, K. Leung, D.J. Burns, Residual Stresses in Autofrettaged Thick-Walled High Pressure Vessels, ASME PVP 110 (1986) 55-60.
[12] A.P. Parker, J.H. Underwood, Influence of the Bauschinger Effect on Residual Stresses and Fatigue Lifetimes in Autofrettaged Thick Walled Cylinders, Fatigue and Fracture Mechanics, 29th Vol. ASTM STP1321. T. L. Panontin and S. D. Sheppard, eds., ASTM, PA, 1998.
[13] H. Jahed, R.N. Dubey, An Axisymetric Method for Elastic-Plastic Analysis Capable of Predicting Residual Stress Field, Trans. ASME, J.Pressure Vessel Tech., 119 (1997) 264-273.
[14] A.P. Parker, J.H. Underwood, D.P. Kendall, Bauschinger Effect Design Procedure For Autofrettaged Tubes Including Material Removal And Sachs' Method," Trans. ASME, J. Pressure Vessel Tech, 121 (1999) 430-437.

[15] A.P. Parker, Autofrettage of open-end tubes – pressure, stresses, strains, and code comparison, Trans. ASME, J. Pressure Vessel Tech., vol. 123 (2001) 271-281.

[16] M. Perl, C. Levy, V. Rallabhandy, Bauschinger Effect's Impact On The 3-D Combined SIFs for Radially Cracked Fully or Partially Autofrettaged Thick-Walled Cylinders, Computer Modeling in Engineering and Sciences: Special Issue on International Workshop on the Advancement of Computational Mechanics, 11 (2006) 37-48.

[17] C. Levy, M. Perl, S. Kotagiri, The Influence of The Bauschinger Effect on 3-D Stress Intensity Factors for Internal Longitudinal Coplanar Cracks in a Fully or Partially Autofrettaged Thick-Walled Cylinder, Eng. Fracture Mech., 73 (2006) 1814-1825.

[18] Q. Ma, C. Levy, M. Perl, The Bauschinger Effect on 3-D SIFs for Networks of Radial and Longitudinally-Coplanar Semi-Elliptical Internal Surface Cracks In Autofrettaged Pressurized Thick-Walled Cylinders, CMES:Computer Modeling in Engineering & Sciences, 927 (2009) 1-16.

[19] Q. Ma, C. Levy, M. Perl, Stress Intensity Factors for Partially Autofrettaged Pressurized Thick-Walled Cylinders Containing Closely and Densely Packed Cracks, Trans. ASME J. Pressure Vessel Tech., 132 (2009), Issue 5, 051203.

[20] Q. Ma, C. Levy, M. Perl, Stress Concentration and Stress Intensity for Pressurized Eroded Autofrettaged Thick Cylinders with Bauschinger Effect, ASME, PVP2010.

[21] Q. Ma, C. Levy, M. Perl, A Finite Element Study of the Effect of Partial Autofrettage on the Fatigue Life of Thick-Walled Cylinders Containing Erosions and Cracks, ASME, PVP2011.

[22] Q. Ma, C. Levy, M. Perl, The Bauschinger Effect's Influence on the SIFs of a Semi-Elliptical Crack Emanating from an Erosion at the Bore of a Fully Autofrettaged Pressurized Cylinder, ASME, PVP2012.

[23] Q. Ma, C. Levy, M. Perl, The Combined Effect of a Finite Axial Erosion with Bauschinger Modified Autofrettage on the 3D SIFs of Pressurized Cylinders, ASME PVP 2014.

[24] A.A. Becker, R.C.A. Plant, A.P. Parker, Axial Cracks in Pressurized Eroded Autofrettage Thick Cylinders, Int. J. Fract., 63 (1993) 113–134.

[25] R.S. Barsoum, On the Use of Isoparametric Finite Elements in Linear Fracture Mechanics, Int. J. Num. Meth. in Eng., 10 (1976) 25- 37.

[26] H. Okada, T. Kamibeppu, A Virtual Crack Closure-Integral Method (VCCM) for Three-Dimensional Crack Problems Using Linear Tetrahedral Finite Elements, CMES: Computer Modeling in Engineering & Sciences, 10 (2005) 229-238.

[27] Sw anson Analysis System Inc., ANSYS 12 User Manual, 2009.

[28] S.L. Pu, M.A. Hussain, Stress Intensity Factors for Radial Cracks in a Partially Autofrettaged Thick-Walled Cylinder, Fracture Mechanics: Fourteen Symposium-Vol. I: Theory and Analysis, eds. J. C. Lewis and G. Sines, ASTM-STP 791 (1983) I-194- I-215.

[29] M. Perl, R. Arone´, Stress Intensity Factors for a Radially Multicracked Partially Auto- frettaged Pressurized Thick-Walled Cylinder, Trans. ASME J. Pressure Vessel Tech.,110 (1988) 147–154.

[30] M. Perl, The Temperature Field for Simulating Partial Autofrettage in an Elasto-Plasic Thick-Walled Cylinder, Trans. ASME, J. Pressure Vessel Tech., 110 (1988) 100-102.

[31] M. Perl, C. Levy, J. Pierola, Three-Dimensional Interaction Effects in an Internally Multicracked Pressurized Thick-Walled Cylinder — Part I: Radial Crack Arrays, Trans. ASME J. Pressure Vessel Tech., 118(3), (1996), pp. 357–363.

[32] C. Levy, M. Perl, and N. Kokkavessis, Three-Dimensional Interaction Effects in an Internally Multicracked Pressurized Thick Walled Cylinder —Part II: Longitudinal Coplanar Crack Arrays, Trans. ASME J. Pressure Vessel Tech., vol. 118(3), (1996), pp. 364–368.

[33] Q. Ma, C. Levy, M. Perl, The Bauschinger Effect's Influence on the SIFs of a Semi-Elliptical Crack Emanating from an Erosion at the Bore of a Fully Autofrettaged Pressurized Cylinder, ASME J. Pressure Vessel Tech, DOI: doi:10.1115/1.4029018, November 03, 2014.